scientific reports

Check for updates

OPEN

Mechanical and dielectric properties of $(ZnSn)_{1-x}M_xO$ (M = Co, Cu) quaternary nanocomposites for promising applications

Mansour Mohamed[1], Emad K. Jaradat[2], A. Sedky[3]✉ & A. G. Abd-Elrahim[3,4]✉

This study investigates the mechanical, elastic wave, AC conductivity, and dielectric properties of $(ZnSn)_{1-x}M_xO$ nanocomposites (NCs), where M is Co or Cu ($0.00 < x < 0.50$), and compares them to those of ZnO and SnO nanosheets. Both Co and Cu series NCs showed minor changes in mechanical and elastic wave propagation up to $x = 0.30$. ZnSnO NCs exhibited higher AC conductivity and dielectric constants than ZnO or SnO nanosheets, which were subsequently reduced by incorporating Co or Cu ions. While ZnSnO NCs displayed high dielectric loss (tan δ), Co incorporation led to lower tan δ without affecting the quality factor (Q_{factor}); conversely, Cu significantly decreased tan δ and strongly improved the Q_{factor}. The conduction mechanism shifted from polaron in ZnO or SnO nanosheets to hole-dominated in ZnSnO and Co-doped ZnSnO NCs, whereas the Cu-doped ZnSnO NCs exhibited a mixed polaron and hole conduction depending on the incorporated Cu content. ZnSnO NCs demonstrated lower bulk impedance and electronic polarizability than binary ZnO and SnO nanosheets; however, doped ZnSnO NCs with high Co concentration dramatically increased both, a trend opposite to that observed with Cu. Effective capacitance (C_{eff}) was significantly enhanced in ZnSnO NCs relative to binary ZnO and SnO nanosheets, followed by C_{eff} decrease with the addition of Co or Cu ions. Conversely, the electric modulus of ZnSnO NCs was considerably reduced compared to SnO or ZnO nanosheets, and this reduction was further amplified by Co or Cu incorporation. Parameters such as polaron binding energy and hopping distance were estimated using the correlated barrier polaron hopping modelVariations in properties between nanosheets and NCs are primarily attributed to differences in internal structures. Notably, these $(ZnSn)_{1-x}M_xO$ NCs, both undoped and doped with Co or Cu, show promise for energy storage applications.

Keywords ZnO and SnO nanosheets, Quaternary transition metal oxide nanocomposites, Mechanical properties, Elastic properties, AC conductivity, Dielectric properties

The non-stoichiometry of n-type ZnO semiconductors primarily arises from oxygen vacancies (Ov), which introduce donor states just below the conduction band (CB) [1,2]. Similarly, p-type SnO can be oxidized into higher-order oxides such as Sn_2O_3 and SnO_2 due to the compensation of native defects, oxygen vacancies and Sn interstitials by free electrons [3,4]. Despite its poorer electrical performance compared to ZnO, SnO remains essential for applications requiring low power consumption, high operation frequency, and circuit reliability [5,6]. However, individual transition-metal oxides (TMsO) often exhibit limitations that restrict their use in advanced electronics. To overcome these deficiencies, hybrid nanocomposites (NCs) composed of two or more TMsO can be engineered. These NCs leverage interfacial charge transfer between different oxides to fine-tune their electrical and physical properties [7–10].

ZnO and SnO nanosheets display versatile functional properties, making them promising candidates for communications systems, high-frequency antennas, Li-ion batteries, supercapacitors, and solar energy conversion devices [11–14]. Integrating SnO into ZnO to form ZnSnO NCs enhances ZnO's carrier mobility, although excess Sn content can lead to interstitial occupation and the formation of neutral defects [15]. Notably, existing literature is predominantly focused on SnO_2-doped ZnO, with limited studies on SnO itself [16–18].

[1]Department of Physics, College of Science, University of Hail, P.O. Box 2440, Hail, Saudi Arabia. [2]Department of Physics, Faculty of Science, Imam Mohammad Ibn Saud Islamic University (IMSIU), Riyadh 11623, Saudi Arabia. [3]Physics Department, Faculty of Science, Assiut University, Assiut 71516, Egypt. [4]School of Mechanical Engineering, University of Ulsan, Ulsan 44610, Korea. ✉email: sedky196000@hotmail.com; ahmed_galal@aun.edu.eg

Cobalt ions (Co^{2+}), with an ionic radius of 0.065 nm, are suitable dopants for replacing either Zn (0.074 nm) or Sn (0.093 nm), owing to their smaller ionic size [19–21]. The incorporation of Co can also enhance surface charge through the formation of Co_3O_4 when Co^{2+} is oxidized to Co^{3+}, or through electron transfer from O^{2-} to Co^{2+} or Co^{3+} [22–24]. Similarly, Cu ions (0.073 nm) closely match the ionic radius of Zn and offer multiple oxidation states, Cu^{+}, Cu^{2+}, and Cu^{3+}, enabling both p-type and n-type doping [25,26]. Transitions from Cu^{2+} to Cu^{+} facilitate electron localization at surface defects in ZnO and SnO matrices [27]. Thus, tailoring the composition of ZnSnO NCs with Co or Cu doping up to substitution levels of 0.50 creates a promising class of $(ZnSn)_{1-x}M_xO$ NCs (M = Co or Cu).

Lattice vibrations in solid-state materials, detectable via Fourier-transform infrared (FTIR) spectroscopy, are critical for applications including optical Kerr shutters (OKS), switching devices, and infrared detectors [28,29]. FTIR analysis reveals insights into carrier concentration and defect-related spin vacancies, with characteristic absorption bands linked to TMs through interatomic vibrations, and the stretching/deformation of adsorbed H_2O [30]. Mechanical properties such as Debye temperature, Poisson's ratio, elastic modulus, hardness, and acoustic wave velocity can also be extracted [31,32].

The presence of multiple valence states in TMsO lattices suggests a polar-ionic conduction mechanism facilitated by electron hopping and defect interactions [33,34]. This mechanism is characterized by complex dielectric constants (ε′ and ε″) across frequencies up to 20 GHz [8]. NCs exhibiting high ε′ are beneficial for communication technologies, while those with lower ε′ are suited for nonlinear optical and high-frequency antenna applications [7,35].

According to Koop's theory, solid NCs comprise highly conducting grains separated by less conductive grain boundaries, leading to frequency-dependent conduction behavior [36,37]. Additionally, Jonscher's power law supports a hopping conduction model with non-Debye relaxation, an important factor for solar cell efficiency [38]. NCs with a dielectric constant on the order of 10^6 and dielectric loss near 10 are promising for energy storage applications and efficient dielectric response [39,40]. Quality (Q_{factor}) and fill (F_{factor}) factors serve as metrics of performance in supercapacitors and solar cells, with Q-factors reaching up to 10,000 at 1 MHz [41,42].

Doping ZnO with transition metals alters its dielectric properties and ac conductivity through hopping mechanisms [43–45]. Similarly, TM-doped SnO NPs show improved dielectric constant (ε), dielectric loss (tanδ), and ac conductivity (σ_{a_c}) [46,47]. Cole–Cole plots confirm grain-boundary dominated conduction, whereas ZnO-doped SnO_2 NCs exhibit reduced ε and tanδ with increasing frequency and temperature [48,49].

Our previous studies explored the effects of Cu and Co doping on the structural, optical, and magnetic properties of ZnSnO NCs [50,51]. Cu doping yielded a mixture of nanosheets and nanorods, while Co doping resulted in uniform nanocube morphology. Both dopants reduced the band gap and enhanced room temperature ferromagnetism. In this work, we extend our investigation to the mechanical and dielectric properties of ZnSnO NCs as influenced by Co and Cu concentrations. For comparative purposes, the properties of pure ZnO and SnO NSs are also assessed. To our knowledge, no comprehensive sequence-based study on these NCs has been reported.

Experimental details

Hydrothermal synthesis of $(ZnSn)_{1-x}M_xO$ NCs

The synthesis and characterization of ZnO and SnO nanosheets, along with $(ZnSn)_{1-x}M_xO$ NCs, where M = Co or Cu, using a facile hydrothermal process, were reported in our previous work. In that study, the influence of Co and Cu concentrations on the structural, optical, and magnetic properties of $(ZnSn)_{1-x}M_xO$ NCs was examined in detail [50,51]. In this experiment, $(ZnSn)_{1-x}M_xO$ nanocomposites (NCs), where M = Co or Cu and x = 0.1–0.5, were synthesized via a hydrothermal method using $ZnCl_2{\cdot}6H_2O$, $SnCl_2{\cdot}2H_2O$, $CuCl_2{\cdot}6H_2O$, and $CoCl_2{\cdot}6H_2O$ as precursors. The procedure involved: (a) dissolving 1 M NaOH in 20 mL of double-distilled water with magnetic stirring at room temperature for 30 min; (b) preparing 1 M metal salt solutions in 20 mL of double-distilled water according to stoichiometric ratios; (c) gradually adding NaOH to the metal solution under constant stirring to form hydroxide precipitates within 1 h; (d) transferring the precipitate to a Teflon-lined autoclave and heating at 140 °C for 12 h, followed by natural cooling to room temperature; (e) washing the resulting powder with ethanol and distilled water, then drying at 400 °C for 3 h.

Lattice vibration and dielectric properties characterization

FTIR spectra of the nanopowders were recorded in the 400–4000 cm^{-1} range at a scan rate of 2 $cm{\cdot}s^{-1}$ using a Nicolet iS10 spectrometer. The experimental density (ρ_{exp}) of the nanocomposites (NCs) was measured via the water displacement method. Water density (ρ_w) was calculated using $\rho_w = m_w/V_w$, where m_w and V_w are the mass and volume of water, respectively. A 0.5 g sample (m_s) was placed in a 5 mL flask filled with water. The displaced water mass was determined by $m_w = m_t - m_s$, and its volume as $V_w = m_w/\rho_w$. The sample volume (V_s) was estimated as $V_s = 5 - V_w$, and its density computed using $\rho_s = m_s/V_s$. Dielectric behavior was analyzed at room temperature using a high-resolution Alpha analyzer and a Novo Control broadband dielectric converter within 100 mHz–20 MHz. The composite powders were finely ground, thoroughly mixed, and compressed into disc-shaped pellets with a diameter of 1 cm and a thickness of approximately 0.3 cm using a hydraulic pressure of 5 tons and positioned between gold-plated stainless-steel electrodes for measurement.

Results and discussion

FTIR analysis

Figure 1a shows FTIR spectra of ZnO, SnO nanosheets, ZnSnO NCs, and $(ZnSn)_{1-x}M_xO$ NCs (M = Co or Cu) at different composition ratios. The FTIR spectrum of ZnO nanosheets exhibited several active vibrations at 455, 695, 1410, 1624, 2367, 2926, and 3440 cm^{-1}. The observed bands at 455 and 695 cm^{-1} are induced by the

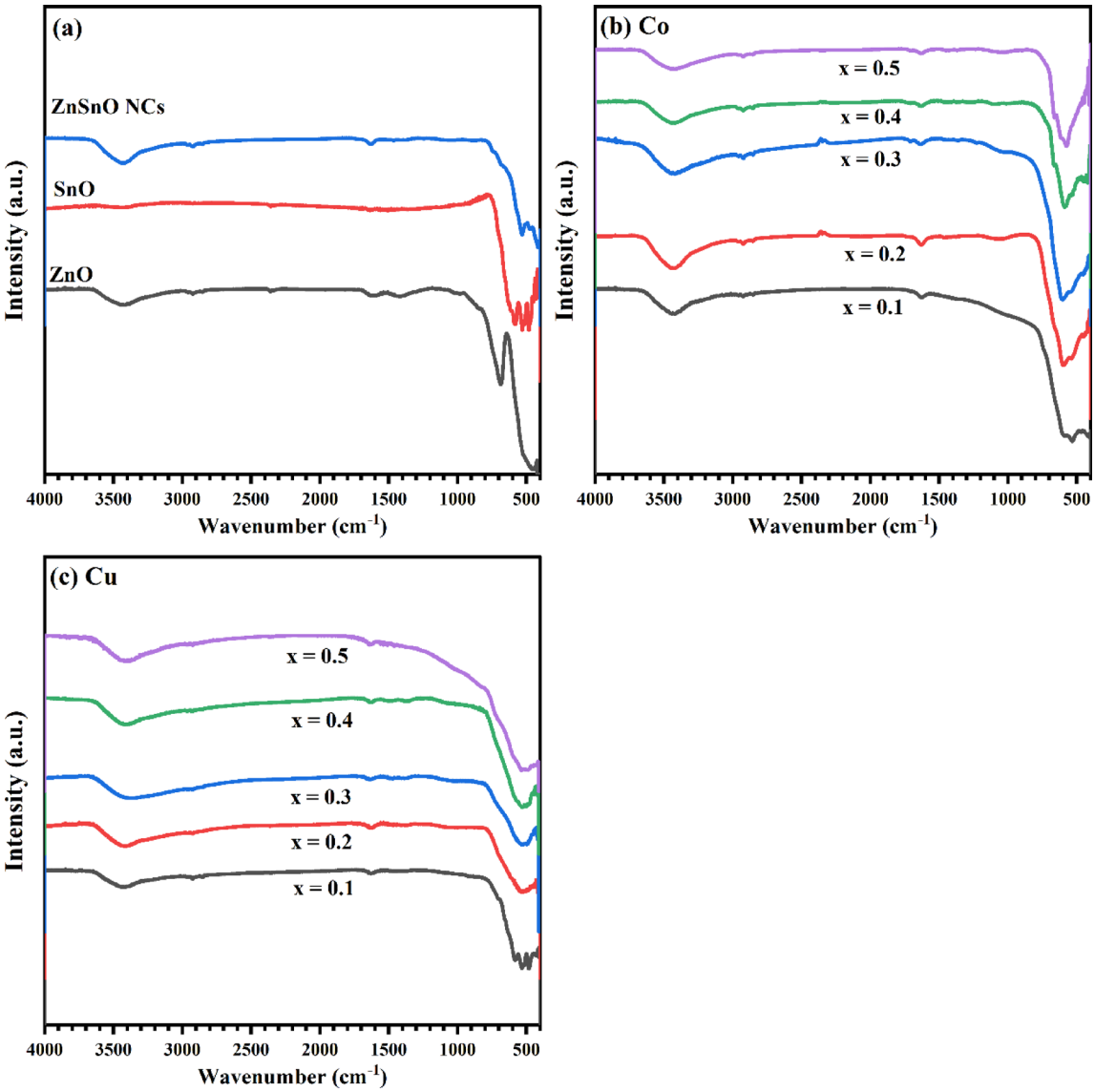

Fig. 1. FTIR spectra of ZnO, SnO nanosheets, and ZnSnO NCs (**a**), $(ZnSn)_{1-x}Co_xO$ (**b**), and $(ZnSn)_{1-x}Cu_xO$ NCs (**c**).

stretching vibrations of Zn–O bonds in hexagonal ZnO structure [52,53]. On the other hand, the characteristic vibrations induced by OH bending and stretching of adsorbed water molecules were detected at 1410 and 3440 cm^{-1}, respectively [54]. Other detected vibrations at 1624, 2367, and 2926 cm^{-1} could be ascribed induced by the vibration of various carbonyl groups induced by the adsorbed CO_2 from surrounding [55]. The FTIR spectrum of SnO nanosheets exhibited several bands at 482, 527, and 590 cm^{-1} that distinguish various stretching vibrations of the Sn–O bond [7,56,57]. The FTIR spectrum of ZnSnO NCs exhibited multiple vibrations at 420, 530, 1620, 2926, and 3440 cm^{-1} that matched with detected modes in either ZnO or SnO nanosheets. Figure 1b exhibits FTIR spectra of Co-series NCs at varying Co content. It was observed that the characteristic vibrations of absorbed OH and CO_2 on the surface of Co-series NCs were slightly affected by replacing (Zn-Sn) ions with Co. However, there was an observable change in the characteristic TM–O bonds vibration with changing Co or Cu-content. The fundamental stretching TM–O vibrations of Co-series NCs were detected at 575, 595, 605, 585, and 570 cm^{-1} corresponding to Co ratio (x) of 0.1, 0.2, 0.3, 0.4, and 0.5, respectively. Figure 1c exhibits FTIR spectra of Cu-series NCs at different Cu content, where the average TM–O stretching vibration at Cu content of 0.1, 0.2, 0.3, 0.4, and 0.5 was detected at 533, 533, 517, 515, 507 cm^{-1}, respectively.

Various mechanical parameters of the micro-crystalline lattice could be estimated from the Debye temperature (θ_D) of the main stretching lattice vibration mode according to the relation [58,59]:

$$\theta_D\,(K) = \frac{hc\overline{\Delta\nu}}{K_B} = 1.44\overline{\Delta\nu} \quad (1)$$

where $\Delta\overline{\nu}$ refers to the average wavenumber (cm^{-1}) of the TM–O stretching vibration band, h is Planck's constant (6.625×10^{-27} erg·s), c light speed (3×10^{10} cm·s^{-1}), and K_B is Boltzmann constant (1.38×10^{-16} erg·K^{-1}). Several mechanical parameters were also determined, such as force constant (K_t), NCs porosity (P_S), Poisson's ratio (γ), and stiffness constants (S_{11}, S_{12}), according to the relations [2]:

$$K_t = 0.0076W^2\overline{\Delta\upsilon} \tag{2}$$

$$P_s = \left(1 - \frac{\rho_{exp}}{\rho_{th}}\right) \tag{3}$$

$$\gamma = 0.324(1 - 1.043P_s) \tag{4}$$

where W is the molecular weight, ρ_{exp} and ρ_{th} refer to the average densities based on experimental technique and XRD theoretical value. It is known that γ value could demonstrate the mechanical deformation behavior of materials, where materials with γ values < 0.26 exhibit ductile elastic deformation like metals. Whereas materials with γ > 0.26 are brittle and exhibit plastic deformation such as ceramic-based materials. According to Table 1, ZnO and SnO nanosheets, ZnSnO NCs, and NCs of Co and Cu-series exhibited brittle mechanical deformation behavior since all estimated γ > 0.26. Other mechanical parameters were estimated using the K_t and γ values including Young modulus (Y), shear modulus (G), bulk modulus (β), and hardness (H) are determined by the following relations [60]:

$$S_{11} = \frac{K_t}{a}; S_{12} = \frac{S_{11}\gamma}{1-\gamma} \tag{5}$$

$$Y = \frac{(S_{11} - S_{22})(S_{11} + 2S_{12})}{(S_{11} + S_{12})}; G = \frac{Y}{2(\gamma+1)}; \beta = \frac{S_{11} + 2S_{12}}{3} \tag{6}$$

$$H = \frac{Y(1-2\gamma)}{6(1+\gamma)} \tag{7}$$

According to the estimated values in Table 1, SnO nanosheets are stiffer than ZnO nanosheets because ZnO have a lower Y value. This behavior demonstrates the Y-value increase of ZnSnO NCs relative to ZnO nanosheets. It can be observed that the incorporation of other TMs ions (i.e., Co or Cu) in the internal lattice of ZnSnO NCs induced a slight variation of Y-values and the associated elastic mechanical parameters with changing composition ratios up to 0.30. A further increase in external TMs was associated with an observable reduction in Y-value. This behavior indicated that the incorporation of either Co or Cu ions enhanced the flexibility of ZnSnO NCs lattice. Moreover, the variation of NCs of Co and Cu series mechanical properties is more sensitive to the concentration than the TMs type. By knowing the material's mechanical properties, some of the lattice vibration dynamics parameters such as propagation velocity of longitudinal wave, shear wave, and the corresponding mean velocities according to the following relations [61]:

$$\nu_L = \sqrt{\left(\frac{S_{11}}{\rho_{th}}\right)}; \nu_s = \sqrt{\left(\frac{G}{\rho_{th}}\right)}; \frac{1}{\nu_m^3} = \frac{1}{\nu_L^3} + \frac{1}{2\nu_s^3} \tag{8}$$

	θ_D (K)	P_S	γ	Y × 10^{11} (D/cm^2)	B × 10^{11} (D/cm^2)	G × 10^{11} (D/cm^2)	H × 10^{10} (D/cm^2)	v_L × 10^5 (cm/s)	v_s × 10^5 (cm/s)	v_m × 10^4 (cm/s)
ZnO	596.37	0.071	0.300	6.49	3.86	2.02	2.64	3.93	1.88	2.22
SnO	633.86	0.070	0.300	14.39	8.30	4.48	5.97	5.26	2.53	2.98
ZnSnO	645.92	0.068	0.301	8.87	5.16	2.77	3.67	4.45	2.14	2.52
Co (x)	$(ZnSn)_{1-x}Co_xO$ (Co-series)									
Co (0.10)	720.93	0.041	0.310	8.13	5.06	2.51	3.18	4.41	2.08	2.46
Co (0.20)	743.26	0.071	0.300	8.52	4.92	2.66	3.55	4.35	2.1	2.47
Co (0.30)	726.07	0.071	0.300	8.2	4.73	2.56	3.42	4.32	2.08	2.45
Co (0.40)	693.36	0.083	0.296	7.67	4.30	2.41	3.27	4.11	1.99	2.35
Co (0.50)	657.93	0.083	0.296	6.6	3.70	2.07	2.82	3.81	1.85	2.18
Cu (x)	$(ZnSn)_{1-x}Cu_xO$ (Cu-series)									
Cu (0.10)	698.41	0.096	0.292	9.06	4.91	2.86	3.97	4.48	2.19	2.58
Cu (0.20)	653.25	0.049	0.307	8.56	5.23	2.65	3.40	4.46	2.11	2.50
Cu (0.30)	637.74	0.084	0.296	8.49	4.73	2.67	3.63	4.27	2.08	2.44
Cu (0.40)	681.60	0.175	0.265	7.96	3.54	2.60	4.08	3.91	2.01	2.34
Cu (0.50)	771.43	0.097	0.291	6.57	3.54	2.07	2.89	3.77	1.85	2.17

Table 1. Mechanical and elastic wave propagation properties of ZnO, SnO nanosheets, ZnSnO NCs, and $(ZnS)_{1-x}M_xO$ NCs (M = Co or Cu) at varying composition ratios.

Due to the variation in material stiffness, SnO nanosheets exhibited a higher proportion velocity than ZnO nanosheets and ZnSnO NCs. Besides, incorporating either Co or Cu ions in ZnSnO NCs induced inhabitation in elastic wave propagation velocity, where the reduction in elastic wave propagation was affected by the concentration of transition metal type.

Dielectric analysis

The real and imaginary dielectric constants (ε′, ε″) of materials are used to reveal the ability of the dielectric medium to store electrical energy, which can be expressed mathematically by the quality factor (Q_{factor}). On the other hand, the dielectric loss tangent (tan δ) refers to the thermal dissipation of stored electrical energy within dielectric medium. The tan δ and Q_{factor} could be estimated from the frequency-dependent behavior of ε′ and ε″ according to the following relations [62,63].

$$tan\delta = \frac{\varepsilon''}{\varepsilon'}; Q_{factor} = \frac{1}{tan\delta} \tag{9}$$

Figure 2a, b reveals the frequency-dependent variation of ε′ and ε″ of ZnO and SnO nanosheets, and their hybrid ZnSnO NCs. In general, it can be observed that both ε′ and ε″ have high values in the low-frequency region, followed by a gradual decrease with increasing applied signal frequency. This behavior could be attributed to the enhancement of surface polarization in the low-frequency region due to charge trapping at the interfacial grain boundaries. With increasing the applied signal frequency, the provided energy induces higher oscillation of trapped charges and facilitates interfacial charge transfers. This behavior is associated with the inhibition of charge polarization at high-frequency regions [64,65]. Ternary ZnSnO NCs exhibited higher ε′ and ε″ than nanosheets ZnO and SnO nanosheets, indicating the improvement of surface polarization in the heterostructure NCs compared with the corresponding pure binary phases. The material dielectric properties are mainly determined by the space charge polarization, which is directly related to the migration of mobile charge through hopping between nearby localized state defects [66]. ZnO and SnO nanosheets have different crystal structures; hence, the formation of heterostructure ZnSnO NCs is expected to contain abundant surface defect states at grain boundary interfaces. These defect states alter the distribution of trapping centers, promoting charge displacement and enhancing surface polarizability and dielectric constant under applied field [67,68].

Figure 2c, d exhibits the frequency-dependent variation of ε′ and ε″ of $(ZnSn)_{1-x}Co_xO$ NCs at varying Co content (x), where a slight reduction in ε′ and ε″ of ZnSnO NCs was observed in the low-frequency region with changing x up to 0.40, whereas a strong decrease was observed at a higher x of 0.5. This revealed that incorporating Co-ions in ZnSnO NCs occurred by replacing Zn or Sn ions in bulk lattice sites, which did not strongly affect the dynamics of interfacial defect states. At x = 0.50, Co ions introduced localized defect states as pinning centers, which hindered surface charge migration, reduced surface polarizability, and lowered the dielectric constant compared to ZnSnO NCs.

On the other hand, the variation of ε′ and ε″ with the applied frequency is more sensitive to the composition in the case of ZnSnO NCs doping with Cu shown in Fig. 2e, f. Incorporating Cu into ZnSnO NCs at low concentrations (≤ 0.20) significantly reduced ε′ and ε″. A further increase in Cu content had a milder effect. This indicates that Cu ions are more strongly altered interfacial defect states and surface polarizability than Co ions, with low Cu levels having a greater impact than higher levels.

Figure 3a, b presents the frequency-dependent tan δ and Q-factor plots for ZnO nanosheets, SnO nanosheets, and ZnSnO NCs. ZnSnO NCs exhibit significantly higher energy loss across the entire frequency range, indicating enhanced conductivity and interfacial charge transport due to reduced intermolecular forces. This reduction facilitates changes in dipole orientations and induces polarizability variations under varying electric fields. [69]. Additionally, SnO nanosheets show a pronounced increase in Q-factors throughout the radio frequency range (20 kHz–20 MHz), suggesting strong electromagnetic absorption compared to ZnO nanosheets and ZnSnO NCs, which exhibit minimal absorption across the same range. Figure 3c, d shows the frequency-dependent tan δ and Q-factor plots for $(ZnSn)_{1-x}Co_xO$ NCs. Peaks in the tan δ plots, observed with increasing Co content up to x = 0.30, indicate resonance between the applied electric field and the orientational polarization response at specific frequencies. The tan δ value of $(ZnSn)_{1-x}Co_xO$ NCs decreased below 10 Hz as x increased from 0.1 to 0.4, followed by a recovery at x = 0.5. Overall, Co-doped NCs exhibited lower tan δ than ZnSnO NCs, suggesting suppressed conductivity. This behavior implies that Co ion incorporation strengthens internal molecular forces and reduces thermal energy dissipation from the applied electric field. Meanwhile, the Q-factor appears less sensitive to Co-ion doping concentrations, indicating a more stable energy storage response across the composition range, as shown in Fig. 3d. Figure 3e, f shows tan δ and Q-factor plots for Cu-doped ZnSnO NCs. Cu incorporation significantly reduced tan δ, suggesting stronger intermolecular forces, lower conductivity, and decreased thermal dissipation. At low Cu content (x = 0.10), the Q-factor rose sharply in the radio frequency range but declined with higher concentrations.

Figure 4a, b reveals plots of real impedance (Z′) and imaginary impedance (Z′′) of ZnO and SnO nanosheets, as well as ZnSnO NCs. ZnO and SnO nanosheets exhibited similar impedance characteristics, where very high Z′ and Z′′ values were observed below 100 Hz followed by a gradual decrease at higher frequencies. ZnSnO NCs showed a significant reduction in Z′ and Z′′ values compared to ZnO and SnO nanosheets. Additionally, the Z′ value of ZnSnO NCs was saturated over a long frequency range extended up to 1 MHz, followed by a gradual decrease at higher frequencies. Conversely, Z′′ was slowly increased with an increase in signal frequency up to 1 MHz, followed by a gradual decrease at higher frequencies. The peak frequency of Z′′ is commonly used to identify the relaxation dynamics within dielectric materials, where the relaxation time (τ) can be estimated according to the following relation [70]:

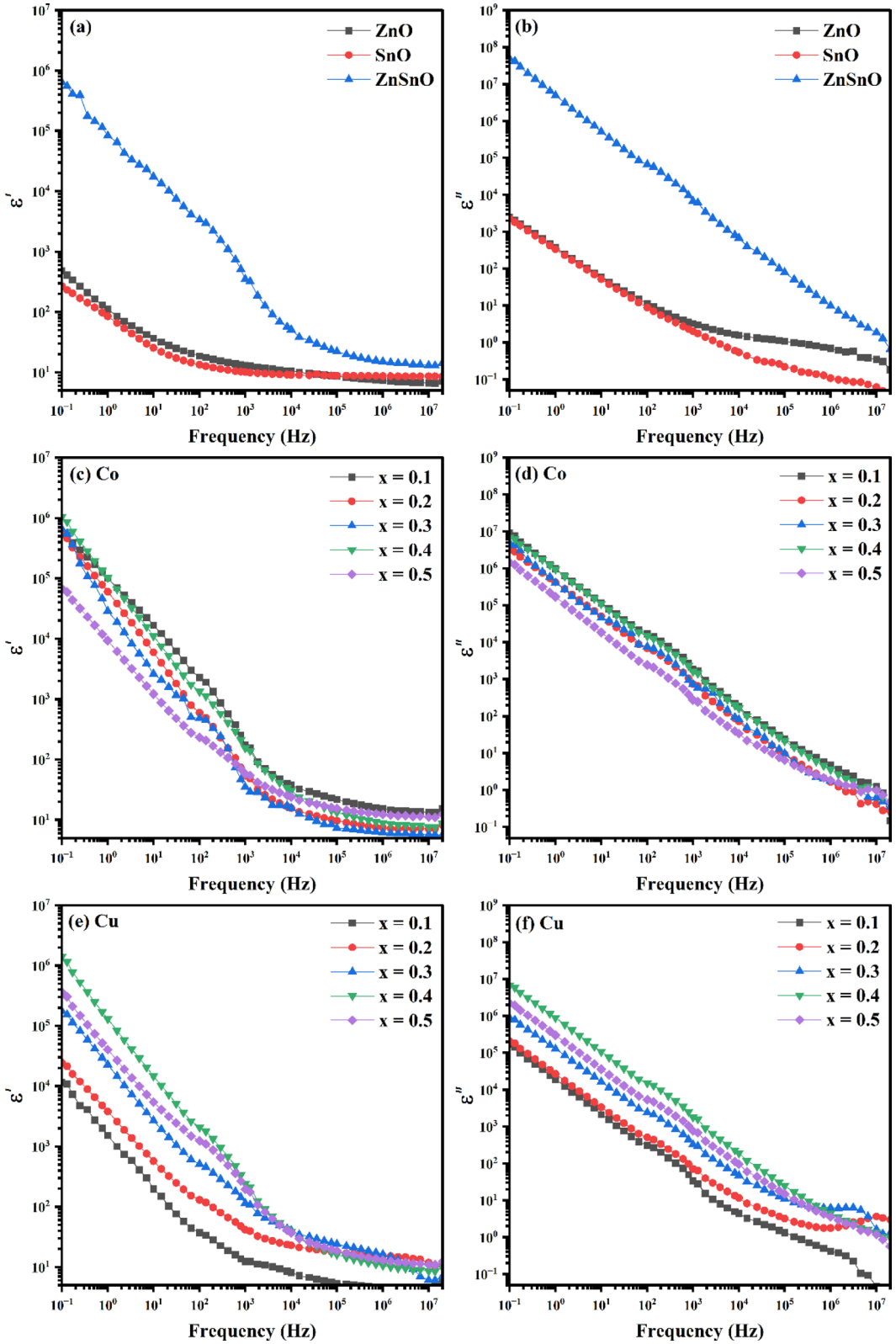

Fig. 2. ε′ and ε″ vs frequency of ZnO, SnO nanosheets, and ZnSnO NCs (**a,b**), $(ZnSn)_{1-x}Co_xO$ NCs (**c,d**), and $(ZnSn)_{1-x}Cu_xO$ NCs (**e,f**).

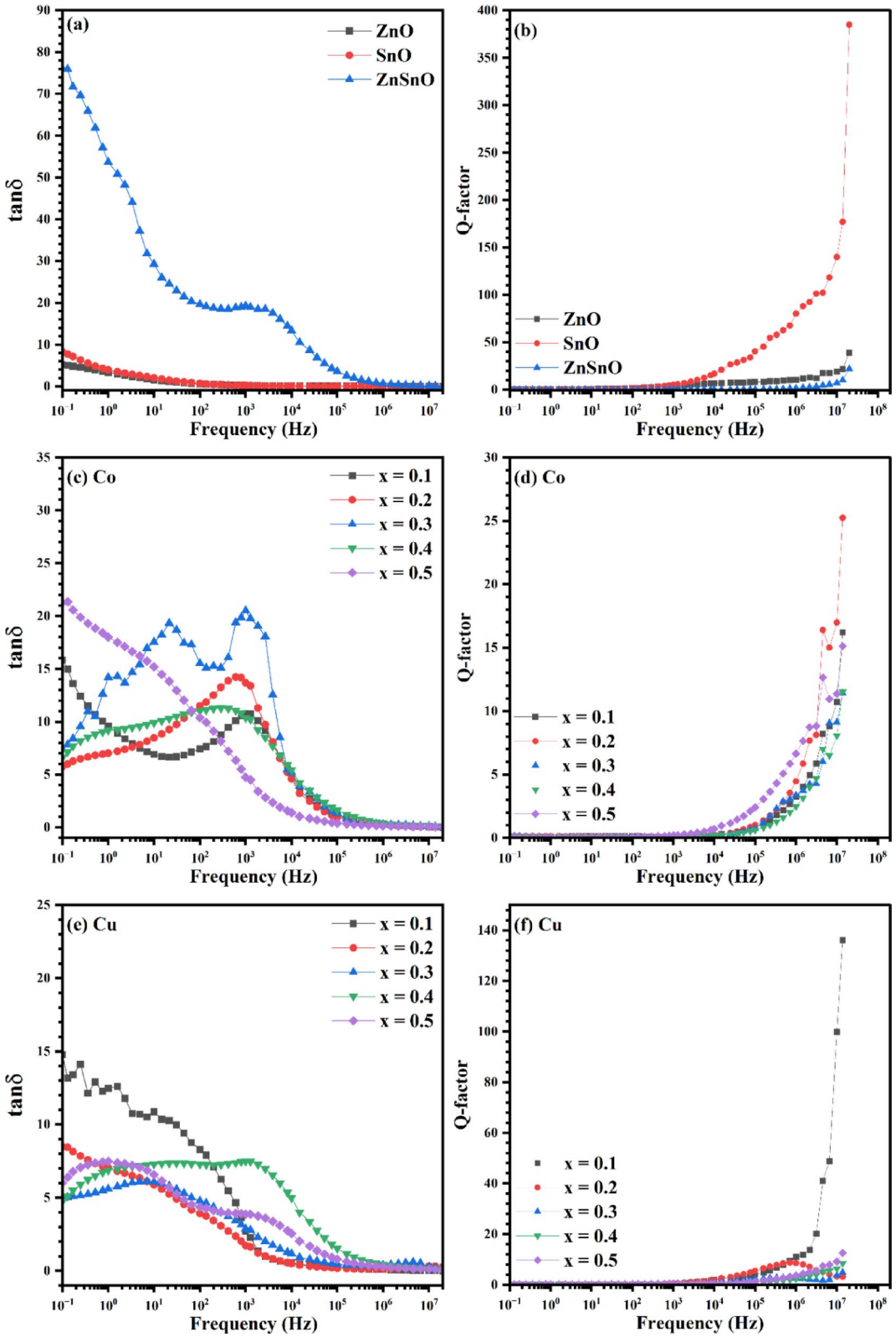

Fig. 3. tan **δ** and Q-factor vs frequency plots of ZnO, SnO and ZnSnO NCs (**a,b**), $(ZnSn)_{1-x}Co_xO$ NCs (**c,d**), and $(ZnSn)_{1-x}Cu_xO$ NCs (**e,f**).

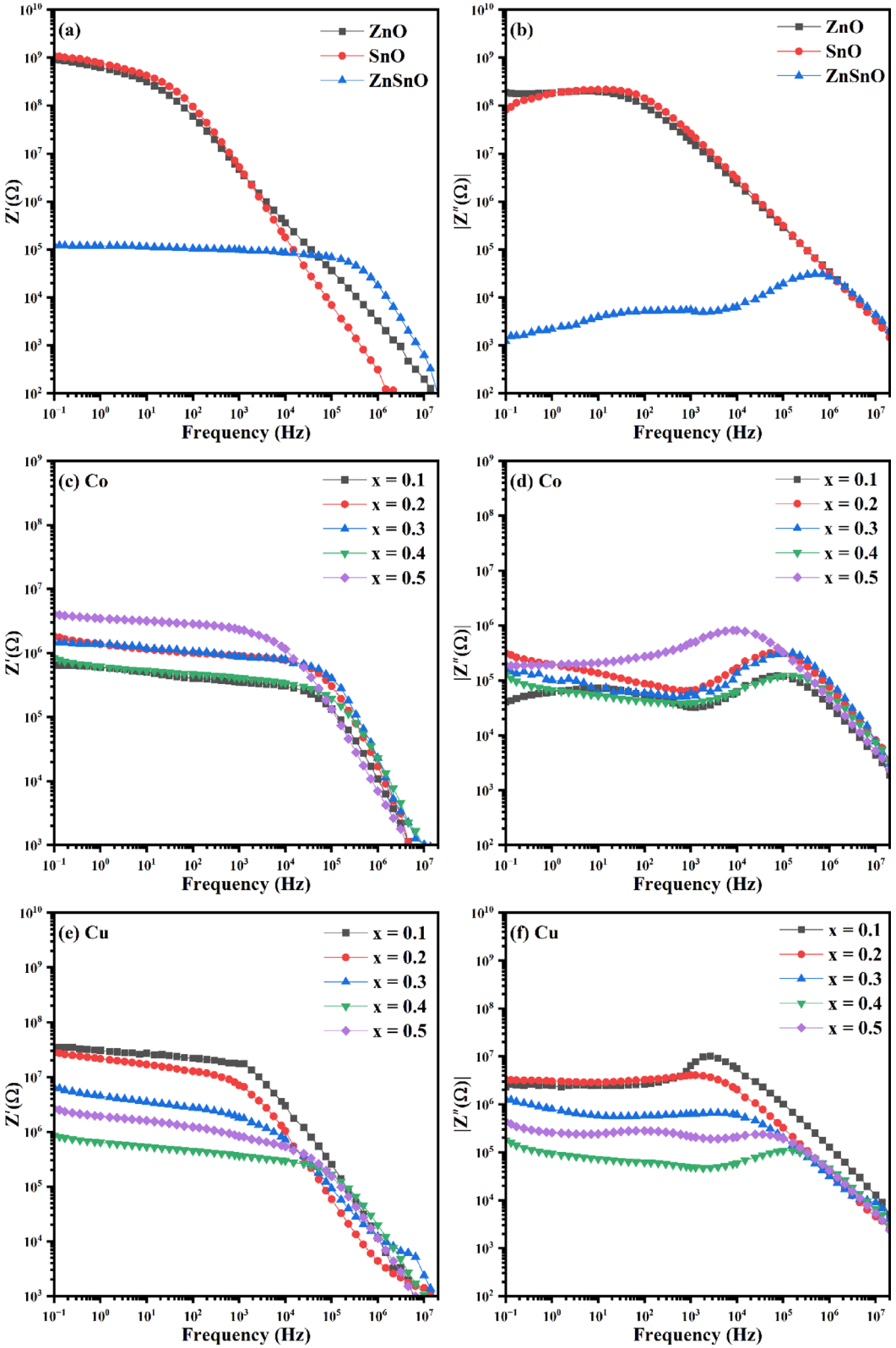

Fig. 4. Plots of Z′ and Z″ vs frequency of ZnO, SnO and ZnSnO NCs (**a,b**), $(ZnSn)_{1-x}Co_xO$ NCs (**c,d**), and $(ZnSn)_{1-x}Cu_xO$ NCs (**e,f**).

$$\tau = \frac{1}{2\pi f_{max}} \tag{10}$$

The estimated τ of ZnO and SnO nanosheets, ZnSnO NCs, and $(ZnSn)_{1-x}M_xO$ NCs (M = Co or Cu) was recorded in Table 2.

It can be observed that ZnSnO NCs have a lower relaxation time than ZnO or SnO nanosheets, demonstrating that ZnSnO NCs have faster relaxation dynamics due to the improvement of interfacial polarization conductivity [71,72]. Figure 4c, d exhibits Z′ and Z′′ plots of $(ZnSn)_{1-x}Co_xO$ NCs at varying Co content, where incorporating Co ions increased Z′ and Z′′ values compared to ZnSnO NCs and shifted the saturation frequency to the lower frequency side. The increase of Co content induced a further increase in Z′ and Z′′ and shifted the saturation frequency to a higher frequency side compared with low Co content. Co-series NCs exhibited higher τ compared with ZnSnO NCs as illustrated in Table 2 Incorporation of Co ions was found to slow the dielectric relaxation of ZnSnO NCs, with higher Co content leading to more pronounced relaxation delays. In contrast, $(ZnSn)_{1-x}Cu_xO$ NCs exhibited a marked increase in Z′ and Z′′ at Cu concentrations of 0.10 and 0.20, followed by a decline at higher levels, as shown in Fig. 4e, f. Additionally, Cu-series NCs displayed a saturation frequency shift toward lower frequencies at Cu content below 0.20, then gradually shifted to higher frequencies with further Cu incorporation, opposite to the trend observed in $(ZnSn)_{1-x}Co_xO$ NCs. Similarly, the incorporation of Cu ions also contributed to slower dielectric relaxation, akin to Co ions. However, in contrast to the Co-series, ZnSnO NCs with lower Cu content exhibited slower relaxation dynamics compared to those with higher Cu levels. This contrasting behavior highlights a strong dependence of the relaxation characteristics on both the type and concentration of transition metal dopant ions in ZnSnO NCs.

Figure 5 shows the Cole–Cole plots of ZnO and SnO nanosheets, ZnSnO NCs, and $(ZnSn)_{1-x}M_xO$ (M = Co or Cu) NCs at varying M content. ZnO and SnO nanosheets revealed that a single semicircle represented the bulk impedance of individual grains, as illustrated in Fig. 5a. On the other hand, ZnSnO NCs exhibited smaller bulk impedance compared with ZnO and SnO nanosheets, as well as another impedance component representing the interfacial grain boundary, as illustrated in Fig. 5b. High Co concentration in doped ZnSnO NCs led to a significant increase in impedance, whereas low Cu content induced higher impedance than high Cu content, as shown in Fig. 5c, d. The real impedance components of bulk grains (Z′(g)) and grain boundaries (Z′(gb)) were extracted from the Cole–Cole plots and summarized in Table 2. Additional parameters, including bulk resistance (R_B) and effective capacitance (C_{eff}) were derived from the frequency-dependent behavior of real impedance (Z′(ω)) according to the following relation [73]

$$Z\prime(\omega) = \frac{R_B}{1 + (\omega C_{eff} R_B)^2} \rightarrow \frac{1}{Z\prime} = \frac{1}{R_B} + \omega^2 C_{eff}^2 R_B \tag{11}$$

ZnSnO NCs exhibited a pronounced reduction in R_B compared to ZnO and SnO nanosheets (Table 2). Co-doping at low concentrations (< 0.20) increased R_B relative to pure ZnSnO NCs, but higher Co content led to a decrease. In contrast, Cu-doped ZnSnO NCs showed R_B values higher than undoped ZnSnO but lower than Co-doped variants. These trends suggest that Co and Cu ions introduce localized structural defects that hinder charge transport and elevate bulk impedance. Notably, ZnSnO NCs displayed a substantial increase in C_{eff} to 0.491 μF and a low R_B of 1300 kΩ, attributed to enhanced surface polarization and hopping conductivity. Both Co and Cu doping restricted interfacial charge movement, resulting in lower C_{eff} than in undoped ZnSnO, as shown in Table 2. For energy storage applications, Li-ion batteries require a small R_B and low C_{eff}, while

	τ (ms)	Z′(g)	Z′(gb)	R_B	C_{eff} (μF)	s	W_m(eV)	$\alpha_e \times 10^{-24}$(cm^{-3})
		$\times 10^5$ (Ω)						
ZnO	3.54	4150	10,400	10,000	0.000224	0.77	0.684	3.98
SnO	3.54	4270	12,000	11,100	0.0001.64	0.68	0.485	3.93
ZnSnO	0.0003	0.264	0.99	1.3	0.491	0.11	0.174	3.59
Co (x)	$(ZnSn)_{1-x}Co_xO$ NCs (Co-series)							
Co (0.10)	0.002	5.94	1.50	333	0.016	0.21	0.197	5.94
Co (0.20)	0.002	4.70	3.77	250	0.028	0.21	0.197	4.70
Co (0.30)	0.002	4.01	4.05	50	0.035	0.28	0.216	4.01
Co (0.40)	0.001	4.48	1.63	10	0.224	0.20	0.194	4.48
Co (0.50)	0.001	4.61	11.5	25	0.045	0.41	0.263	4.61
Cu (x)	$(ZnSn)_{1-x}Cu_xO$ NCs (Cu-series)							
Cu (0.10)	0.086	110	261	5	0.028	0.43	0.272	2.66
Cu (0.20)	0.086	66.30	141	16.7	0.025	0.72	0.555	3.20
Cu (0.30)	0.019	11.60	33.10	14.3	0.075	0.53	0.330	2.71
Cu (0.40)	0.001	1.67	3.63	10	0.224	0.24	0.204	2.93
Cu (0.50)	0.003	2.62	11.90	33.3	0.078	0.31	0.225	3.02

Table 2. τ, Z′ (g), Z′ (gb), R_b, C_{eff}, s, W_m, and α_e parameters of ZnO and SnO *nanosheets*, ZnSnO NCs, and $(ZnSn)_{1-x}M_xO$ NCs (M = *Co or Cu)*.

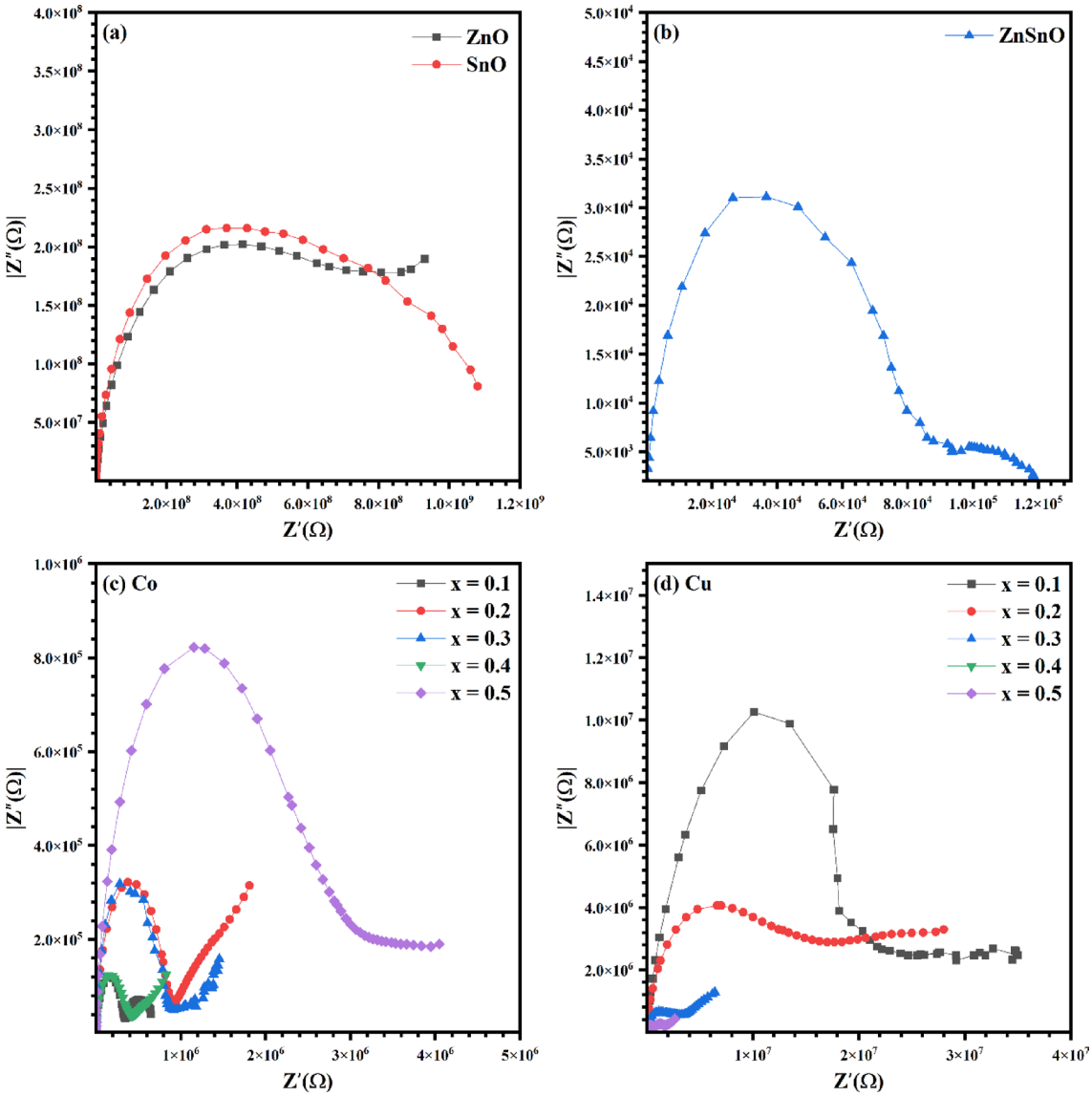

Fig. 5. | Z″| vs Z′ plots of ZnO, SnO and ZnSnO NCs (**a**), $(ZnSn)_{1-x}Co_xO$ NCs (**b**), and $(ZnSn)_{1-x}Cu_xO$ NCs NCs (**c**).

supercapacitors favor low R_B and high C_{eff} [74]. Accordingly, pure ZnSnO and NCs doped with 0.40 Co or Cu are suited for supercapacitors, whereas NCs with 0.10 Cu are better candidates for Li-ion batteries.

The impact of Co and Cu ions incorporation on the polarization conduction mechanism of ZnSnO NCs at room temperature (RT) was investigated across the applied frequency range. The total conductivity (σ) of the material arises from the frequency-independent DC conductivity (σ_{DC}) and the AC conductivity (σ_{AC}), which varies with the frequency of the applied electric field according to the relations [74,75]:

$$\sigma_t(\omega) = \sigma_{dc} + \sigma_{ac} = \sigma_{dc} + B\omega^s \tag{12}$$

where B, ω, and s represent proportionality constant, angular frequency, and exponent factor, respectively. The contribution of σ_{AC} in the total conductivity sharply increases with increasing frequency due to the strong improvement of charge carrier mobility [76]. The hopping mechanism of charge transfer between interfacial defect states could be identified through the s-value, where the hopping mechanism is mainly caused by holes when $0 < s < 0.50$, whereas electron conduction is dominant when $0.50 < s \leq 1.00$ [77]. Figure 6a, b illustrate the variation in σ_{AC} as a function of frequency, and $\ln\sigma_{AC}$ vs $\ln\omega$ plots for ZnO and SnO nanosheets as well as ZnSnO NCs. It was observed that the σ_{AC} gradually increases progressively with rising applied frequency, a characteristic behavior common to all the studied nanomaterials, indicating enhanced charge hopping mobility in the high-frequency region [78]. Besides, ZnSnO NCs exhibited better σ than ZnO or SnO nanosheets because of the development of various interfacial structural defects like vacancies and interstitials in heterostructure NCs. These defect states act as localized trapping centers that facilitate charge transportation by hopping through reducing interfacial

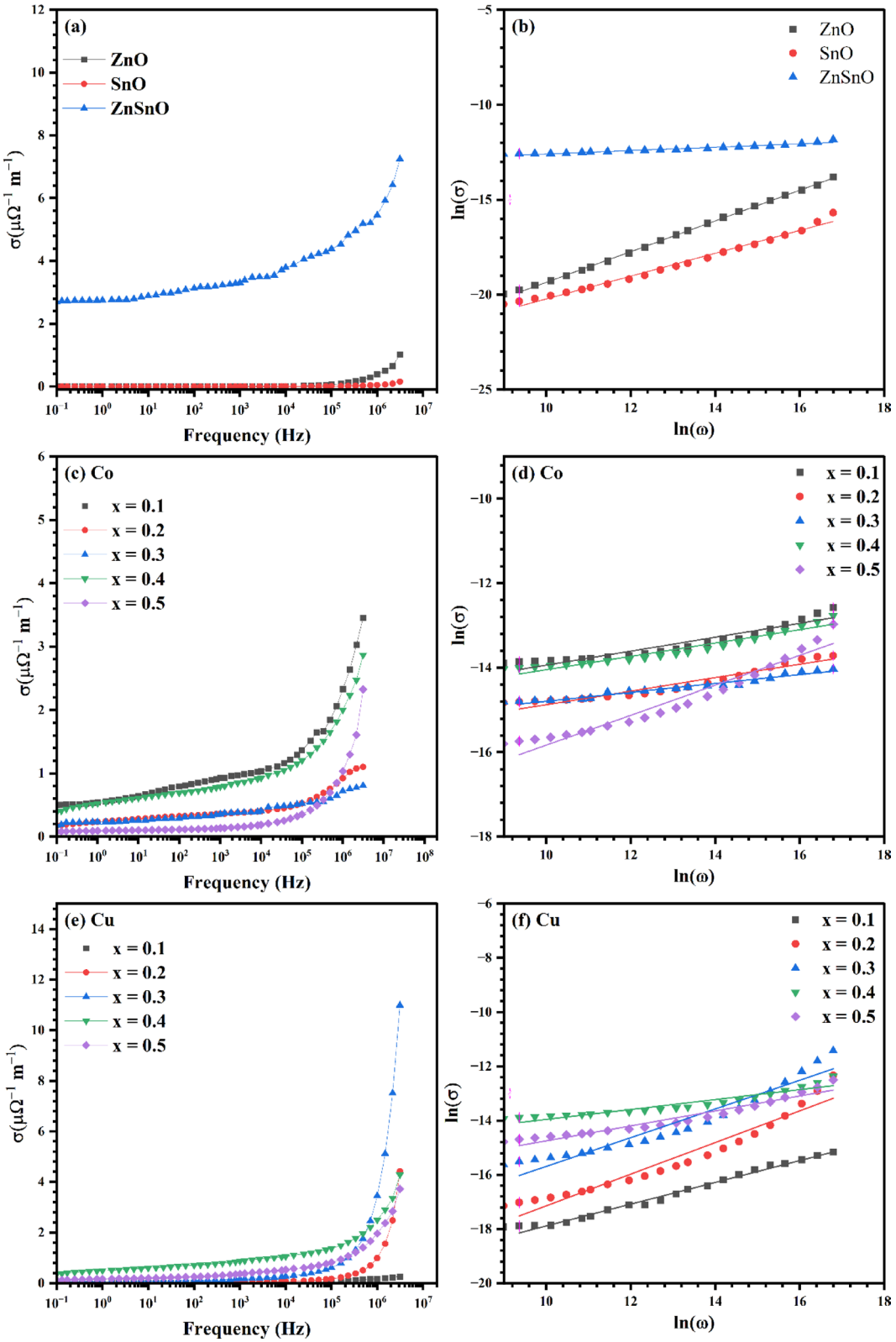

Fig. 6. σ_{AC} and $\ln\sigma_{AC}$ vs frequency plots of ZnO and SnO nanosheets and ZnSnO NCs (**a,b**), $(ZnSn)_{1-x}Co_xO$ NCs (**c,d**), and $(ZnSn)_{1-x}Cu_xO$ NCs (**e,f**).

depletion width. ZnSnO NCs showed higher σ than ZnO and SnO nanosheets, due to interfacial structural defects, such as vacancies and interstitials within the heterostructured NCs. These defects act as trapping centers, enhancing charge hopping by reducing the interfacial depletion width [79]. As listed in Table 2, ZnO and SnO nanosheets exhibited s-values greater than 0.5, indicating that polaron hopping occurred through bound electrons interacting with interfacial localized defect states [80]. In contrast, polaron hopping in heterostructured ZnSnO nanocrystals (NCs) was hole-dominated, reflected by s-values below 0.5.

Figure 6c, d illustrates the plots of σ_{AC} vs frequency and $\ln(\sigma_{AC})$ vs $\ln(\omega)$ for Co-doped ZnSnO NCs, where Co incorporation led to a reduction in σ_{AC} across the entire frequency range. This behavior was associated with the evolution of s-values, which remained below 0.5, confirming that Co doping did not alter the hole-based polaron hopping mechanism in ZnSnO NCs. Figure 6e, f presents similar plots for Cu-doped ZnSnO NCs, which demonstrate a charge transport mechanism highly sensitive to Cu concentration. As shown in Table 2, s-values increased significantly with Cu content up to x = 0.20, suggesting a shift toward electron-dominated hopping, but decreased again at higher doping levels. Accordingly, the hopping mechanism in $(ZnSn)_{1-x}Cu_xO$ NCs at x = 0.20 and 0.30 was primarily electron-driven, unlike samples at other Cu ratios. Additional parameters describing the hopping conduction mechanism were evaluated using the correlated barrier hopping (CBH) model. These parameters include the polaron binding energy (W_m), average hopping distance (R_h), figure of merit (F_m), and the density of interfacial localized defect states (N_D). Their estimation was carried out based on the following mathematical relations [70,81]:

$$W_m = \frac{6K_BT}{1-s}; R_h = \frac{e^2}{\pi\varepsilon_o\varepsilon\prime W_m} \tag{13}$$

$$N_D = \frac{24\sigma}{\pi^3\varepsilon_\circ\varepsilon\prime\omega R_h^6}; F_m = \frac{\sigma}{\varepsilon\prime} \tag{14}$$

The estimated W_m values for ZnO and SnO nanosheets, ZnSnO NCs, and $(ZnSn)_{1-x}M_xO$ NCs, as listed in Table 2, were lower than their respective optical band gaps, as reported in our previous studies [50,51]. This observation confirms that charge transport in Co- and Cu-doped ZnSnO NCs occurs predominantly via a single polaron hopping mechanism [82]. Moreover, the W_m values for Co- and Cu-doped series were higher than those of undoped ZnSnO NCs, indicating that Co and Cu ion incorporation enhances the interaction between interfacial defect states and excited charge carriers.

Figure 7a illustrates the frequency-dependent R_h plots for ZnO and SnO nanosheets, and ZnSnO nanocrystals (NCs). SnO nanosheets exhibited a steady increase in R_h in the low-frequency region (< 1 kHz). Afterwards, R_h became almost saturated and less influenced by the applied signal frequency. In contrast, ZnO nanosheets showed a gradual increase in R_h across all frequencies, with values consistently lower than those of SnO nanosheets. An interesting observation was that ZnSnO NCs displayed frequency-independent R_h behavior below 1 kHz, followed by a sharp increase at higher frequencies. In the high-frequency range, R_h was lower than that of both ZnO and SnO nanosheets. Figure 7b presents the frequency-dependent R_h plots for $(ZnSn)_{1-x}Co_xO$ NCs. Co incorporation between x = 0.20 and 0.40 led to a substantial increase in R_h compared to ZnSnO NCs, while minimal variation was observed at other Co concentrations. Figure 7c shows that introducing Cu at x = 0.10 in $(ZnSn)_{1-x}Cu_xO$ NCs caused a significant increase in R_h relative to both ZnSnO and $(ZnSn)_{1-x}Co_xO$ NCs. Additionally, the R_h response shifted toward lower frequencies compared to ZnSnO NCs. At higher Cu concentrations, R_h decreased, suggesting that x = 0.10 represents a critical composition for optimizing R_h response to applied polarization frequency.

Figure 8a, b illustrates the frequency-dependent behavior of N_D and the corresponding F-factor for ZnO and SnO nanosheets, as well as ZnSnO NCs. The formation of heterostructure interfaces between ZnO and SnO grains in ZnSnO NCs significantly increased N_D and the F-factor compared to either pure ZnO or SnO nanosheets. The variation of N_D with frequency revealed a metastable distribution of interfacial defect states, evidenced by a gradual decline in N_D with increasing sinusoidal frequency. Meanwhile, enhanced polarization conductivity due to charge hopping was reflected in the progressive rise of the F-factor as frequency increased. Figure 8c, d presents the N_D and F-factor plots of Co-series NCs, showing no significant change with Co content up to 0.40. A slight decrease in both values is observed at 0.50 Co content. Figure 8e displays N_D plots of Cu-series NCs, where a sharp drop in N_D occurs at 0.10 Cu concentration compared to ZnSnO NCs, followed by gradual recovery at higher Cu levels. This indicates that low Cu content more strongly influences the distribution of localized defect states than higher concentrations, opposite to the trend seen with Co doping. The F-factor of Cu-series NCs in Fig. 8f also shows a slight decline at 0.10 Cu content, with negligible variation at higher levels.

The electronic polarizability (α_e) could be estimated from the saturated value of the real dielectric constant (ε'_∞) at the high-frequency region based on the Clausius–Mossotti formula given below [83,84]:

$$\alpha_e = \frac{3W_m}{4\pi N_A\rho}\left(\frac{\varepsilon_\infty\prime - 1}{\varepsilon_\infty\prime + 2}\right) \tag{15}$$

where N_A is Avogadro's number.

ZnSnO NCs exhibited lower α_e than pure ZnO and SnO nanosheets, as illustrated in Table 2. Besides, incorporating Co ions strongly enhanced α_e of ZnSnO NCs in contrast to Cu ions that diminished α_e. It was observed that the lowest doping content of Co or Cu (i.e., x = 0.10) produced the highest effect compared with other compositions.

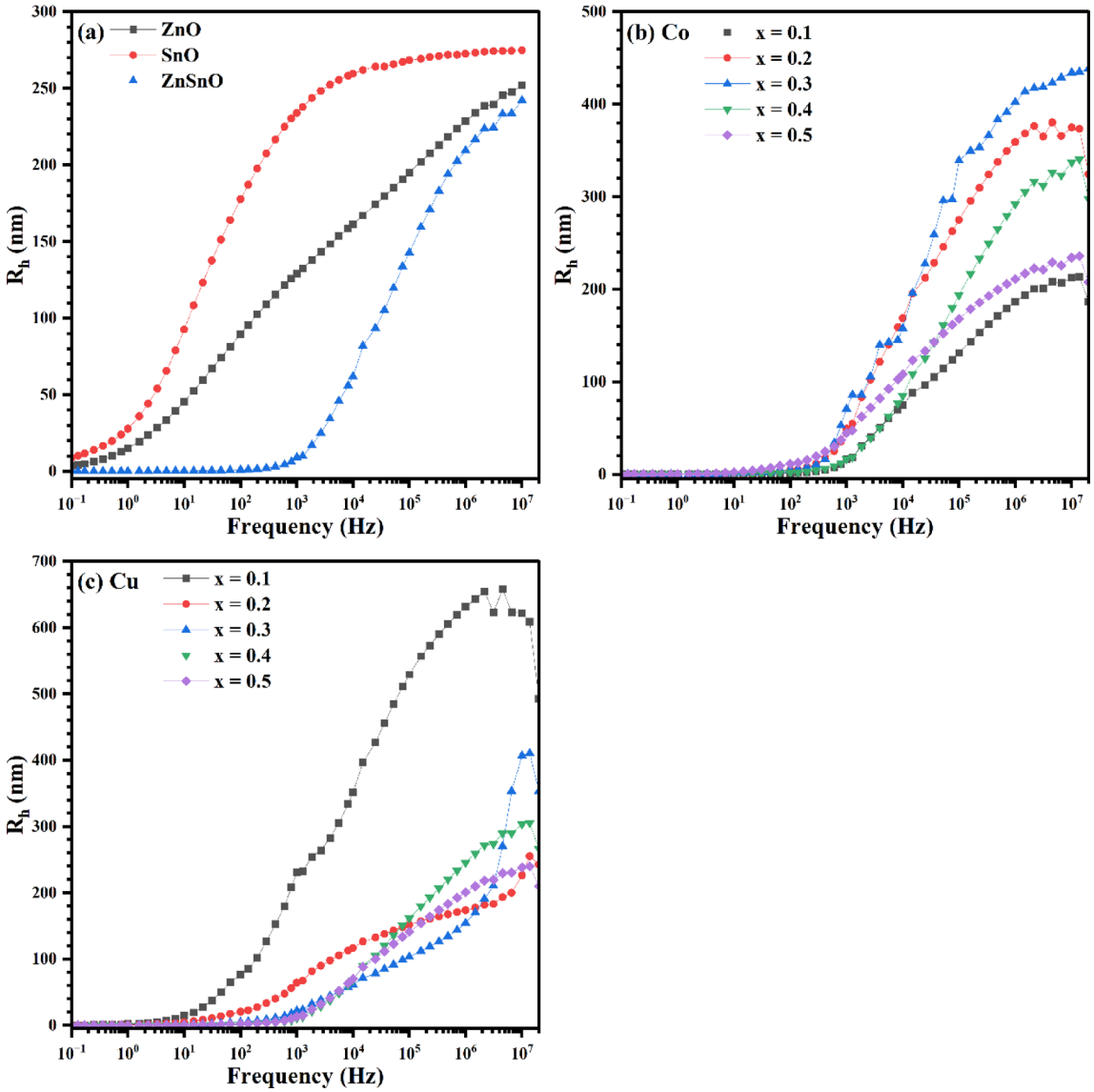

Fig. 7. Plots of R_h vs frequency of ZnO and SnO nanosheets, and ZnSnO NCs (**a**), $(ZnSn)_{1-x}Co_xO$ NCs (**b**), and $(ZnSn)_{1-x}Cu_xO$ NCs (**c**).

The electrical relaxation mechanism in dielectric materials could be investigated through the frequency-dependent features of real (M′) and imaginary (M″) electrical modulus complexes, which offer detailed insights into the charge transport dynamics, as described by the following equations [85]:

$$M\prime = \frac{\varepsilon\prime}{\left((\varepsilon\prime)^2 + (\varepsilon'')^2\right)} \tag{16}$$

$$M'' = \frac{\varepsilon''}{\left((\varepsilon\prime)^2 + (\varepsilon'')^2\right)} \tag{17}$$

Figure 9a, b shows the frequency-dependent M′ and M″ plots of ZnO and SnO nanosheets, and ZnSnO NCs, where a strong reduction in M′ and M″ of ZnSnO NCs compared to pure nanosheets is observed. The M′ of ZnO and SnO nanosheets started to saturate from 100 Hz, whereas saturation started from 1 MHz in the case of ZnSnO NCs.

The observed increase in M′ with rising frequency may be attributed to the conduction of charge carriers with short-range mobility, as well as the diminished restoring force opposing their motion under a steady electric field [86]. On the other hand, the frequency-dependent plot of M″ in Fig. 9b shows that ZnO and SnO nanosheets share a low-frequency relaxation peak followed by semi-saturation at high frequencies, unlike ZnSnO NCs, which show a peak only in the high-frequency range. This behavior suggests that ZnO and SnO nanosheets possess long-range charge mobility, driven by interfacial polarization consistent with the Maxwell–Wagner–Sillars effect [87].

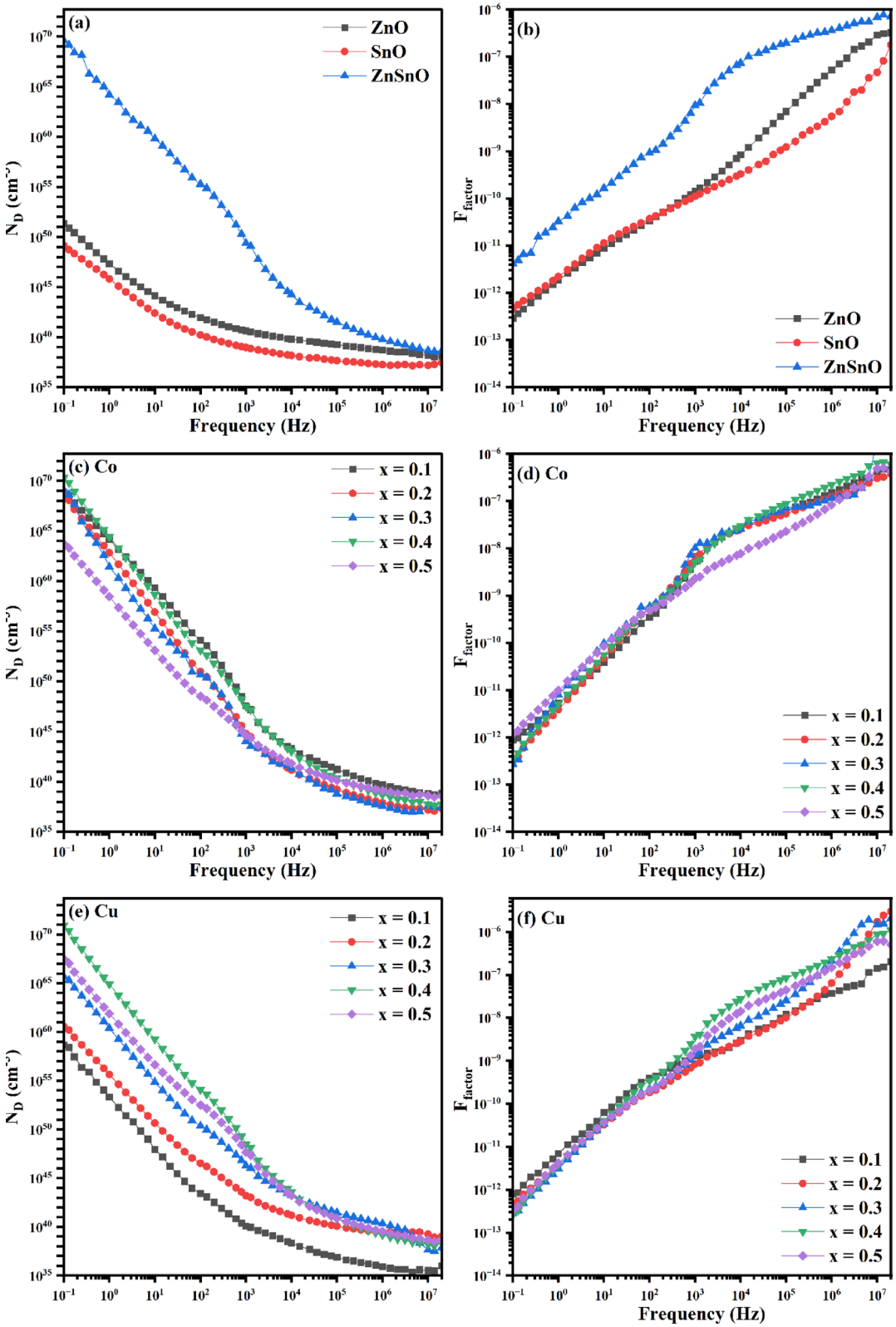

Fig. 8. N_D and F_{factor} vs frequency plots of ZnO, SnO and ZnSnO NCs (**a,b**), $(ZnSn)_{1-x}Co_xO$ NCs (**c,d**), and $(ZnSn)_{1-x}Cu_xO$ NCs (**e,f**).

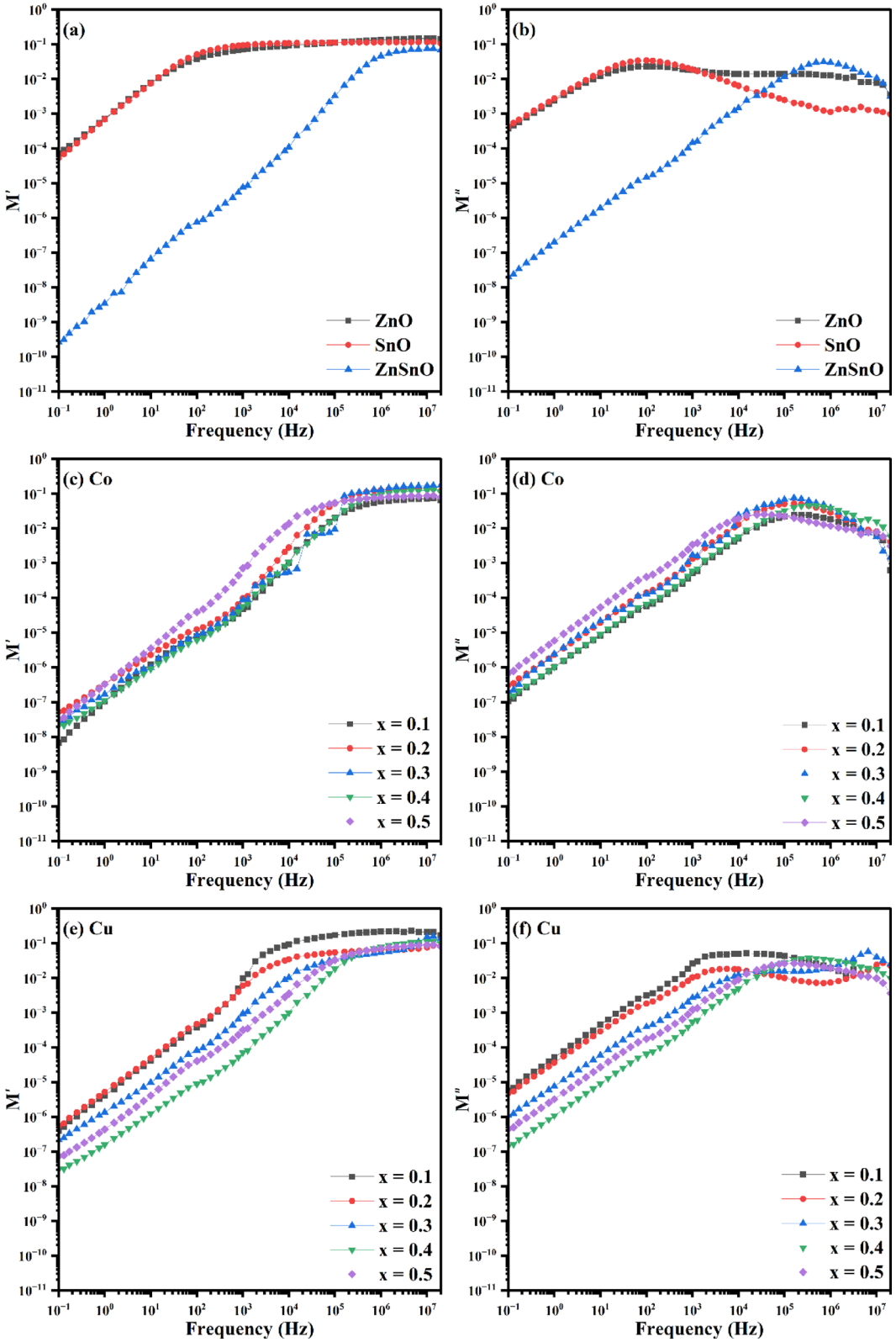

Fig. 9. M′ and M″ vs frequency plots of ZnO and SnO nanosheets, and ZnSnO NCs (**a**,**b**), $(ZnSn)_{1-x}Co_xO$ NCs (**c**,**d**), and $(ZnSn)_{1-x}Cu_xO$ NCs (**e**,**f**).

In contrast, ZnSnO NCs demonstrate only short-range carrier mobility, likely governed by dipolar polarization at the metal oxide grain boundaries [88]. Figure 9c, d demonstrate M′ and M″ plots of $(ZnSn)_{1-x}Co_xO$ NCs, where the addition of Co ions enhanced M′ and M″ of ZnSnO NCs with changing starting frequency of saturation. M′ and M″ plots of Cu-series NCs in Fig. 9e, f showed several composition-dependent features compared to Co-series NCs. A strong improvement in M′ and M″ plots at low Cu content of 0.10 and 0.20, followed by a gradual reduction at higher Cu concentrations, overall, the frequency range. The M′ plots of Co-series NCs at x = 0.10 and 0.20 exhibited saturation starting at a low frequency of 5 kHz compared with ZnSnO NCs (1 M Hz). Besides, the starting frequency of saturation was shifted to higher frequencies with increasing Cu content. Based on the frequency-dependent M″ plots in Fig. 9d, f, both $(ZnSn)_{1-x}Co_xO$ and $(ZnSn)_{1-x}Cu_xO$ nanocomposites exhibit short-range carrier mobility in the high-frequency region, similar to ZnSnO NCs. However, the relaxation peak for $(ZnSn)_{1-x}Cu_xO$ NCs appears at a lower frequency compared to both ZnSnO and $(ZnSn)_{1-x}Co_xO$ NCs. This shift suggests that Cu doping enhances the charge transport dynamics by extending the mobility range, likely due to improved dipolar polarization and reduced interfacial barriers.

Doping ZnSnO nanocrystals (NCs) with Co or Cu ions significantly alters their properties, primarily due to changes in their internal structure, including crystallite and particle sizes, and the formation of specific interfacial grain boundaries; both dopants induce only slight changes in mechanical and elastic wave propagation properties, reduce ϵ and σ_{AC}, and decrease C_{eff}, while generally increasing R_h; however, Co enhances α_e in contrast to Cu ions which enhance M, Co exhibits lower tan δ without affecting the Q factor whereas Cu strongly decreases tan δ with a strong Q factor, Co leads to hole conduction while Cu exhibits polaron or hole conduction relative to its content, and Co induces a strong Z in contrast to Cu whose low content induces higher Z; additionally, increasing Co to 0.50 increases ND and F-factor, while 0.10 Cu content causes a slight decrease. While the crystallite size of ZnSnO NCs is 12.6 nm (between 20.70 nm for SnO and 7.70 nm for ZnO nanosheets), increasing Co up to 0.50 results in slight variations in crystallite size (e.g., 13, 13.2, 9, and 11.56 nm), whereas the Cu series shows a decrease (e.g., 18.45, 14.60, 12.40, 12.10, and 10.50 nm), demonstrating that both Co and Cu inhibit grain growth and induce distinct interfacial grain boundaries, with Co causing a more significant decrease in particle size than Cu at the same molar ratio, and further increasing Co or Cu leads to phase separation, recognizing cubic Co3O4, cubic Cu2O and monoclinic CuO phases were recognized as reported in our previous work [50,51]. These internal structures played a significant role in dictating the variation in the physical properties of $(ZnSn)_{1-x}M_xO$ NCs, with the specific incorporated metal (Co or Cu) determining the outcome. Consequently, some of these $(ZnSn)_{1-x}M_xO$ NCs exhibited better dielectric characteristics compared to ZnO or SnO nanosheets, making them highly suitable for energy-related applications.

Conclusions

The composition-dependent mechanical and dielectric properties of hydrothermally synthesized quaternary $(ZnSn)_{1-x}M_xO$ NCs, where M = Co or Cu, were investigated at room temperature across varying dopant concentrations. SnO nanosheets exhibited higher mechanical coefficients than ZnO nanosheets, indicating superior stiffness, which correlates with decreased elastic wave propagation velocities. Meanwhile, ZnSnO NCs demonstrated intermediate mechanical coefficients and elastic wave velocities relative to those of ZnO and SnO nanosheets, suggesting effective hybridization between Zn and Sn cations within the ternary structure. ZnSnO NCs exhibited higher AC conductivity and dielectric constants compared to ZnO and SnO nanosheets, although Co and Cu doping reduced these properties due to increased defect states. Co lowered tan δ without affecting the Q_{factor}, while Cu improved both tan δ and the Q_{factor} significantly. The conduction mechanism shifted from polaron-based in ZnO and SnO to hole-dominated in ZnSnO and Co-doped variants, with Cu-doped NCs showing mixed conduction behavior. ZnSnO NCs had reduced impedance and polarizability, though high Co content reversed this trend; Cu maintained low values. Effective capacitance was enhanced in ZnSnO NCs but declined with doping, while the electric modulus decreased further upon Co or Cu incorporation. These changes, driven by structural differences and doping effects, highlight the promise of ZnSn-based NCs for energy storage applications.

Data availability

The datasets generated during and/or analysed during the current study are available from the corresponding author on reasonable request.

Received: 26 June 2025; Accepted: 12 September 2025
Published online: 04 November 2025

References

1. Sedky, A., Ali, A. M. & Mohamed, M. Structural and optical investigation of pure and Al doped ZnO annealed at different temperatures. *Opt. Quant. Electron.* **52**, 42 (2020).
2. Al-Naim, A. F., Afify, N., Sedky, A. & Ibrahim, S. Structural morphology and nonlinear behavior of pure and co-doped Zn1-x-yFexMyO varistors with (M= Cu, Ni). *Appl. Phys. A* **127**, 486 (2021).
3. Zhou, W. & Umezawa, N. Band gap engineering of bulk and nanosheet SnO: An insight into the interlayer Sn–Sn lone pair interactions. *Phys. Chem. Chem. Phys.* **17**, 17816–17820 (2015).
4. Alam, M., Asiri, A. M. & Rahman, M. M. Wet-chemically synthesis of SnO2-doped Ag2O nanostructured materials for sensitive detection of choline by an alternative electrochemical approach. *Microchem. J.* **165**, 106092 (2021).
5. Ahn, S.-Y. et al. Performance enhancement of p-type SnO semiconductors via SiOx passivation. *Mater. Today Commun.* **26**, 101747 (2021).
6. Januar, M. et al. Room-temperature fabrication of p-type SnO semiconductors using ion-beam-assisted deposition. *ACS Appl Mater Interfaces* **14**, 46726–46737 (2022).

7. Sedky, A., Afify, N., Hakamy, A. & Abd-Elnaiem, A. M. Structural, optical, and dielectric properties of hydrothermally synthesized SnO2 nanoparticles, Cu/SnO2, and Fe/SnO2 nanocomposites. *Phys. Scr.* **98**, 125929 (2023).
8. Sedky, A. et al. Structural, optical, and dielectric properties of M/SnO2 (M= Al2O3, NiO, Mn3O4) nanocomposites. *Ceram. Int.* **50**, 3409–3421 (2024).
9. Yousefi, R., Azimi, H. R., Mahmoudian, M. R. & Cheraghizade, M. Highly enhanced photocatalytic performance of Zn(1–x) MgxO/rGO nanostars under sunlight irradiation synthesized by one-pot refluxing method. *Adv. Powder Technol.* **29**, 78–85 (2018).
10. Yousefi, R. & Muhamad, M. R. Effects of gold catalysts and thermal evaporation method modifications on the growth process of Zn1–xMgxO nanowires. *J. Solid State Chem.* **183**, 1733–1739 (2010).
11. Ali, A. M. et al. Morphological and optical properties of SnO2 doped ZnO nanocomposites for electrochemical sensing of hydrazine. *Int. J. Electrochem. Sci.* **14**, 1461–1478 (2019).
12. Sedky, A., Amin, S. & Mohamed, M. Electrical, photoluminescence and ferromagnetic characterization of pure and doped ZnO nanostructures. *Appl. Phys. A* **125**, 308 (2019).
13. Sedky, A. et al. Comparative investigation of structural, photoluminescence, and magnetic characteristics of M x Sn1− x O y nanocomposites. *Appl. Phys. A* **129**, 669 (2023).
14. Abd-Elrahim, A. G., Ali, M. A. & Chun, D.-M. Electrodeposition of a novel porous, crystalline Cd-rich CdS nanonoodles on ZnO nanosheets for enhanced solar light-driven water splitting. *J. Power Sources* **655**, 237950 (2025).
15. M.H. Farooq, R. Hussain, L.e. Zhang, I. Aslam, M. Tanveer, M. Shah, M.Z. Iqbal, Fabrication, characterization and magnetic properties of Mn-doped SnO nanostructures via hydrothermal method, Mater. Lett., 131 (2014) 350–353.
16. Li, Y., Zhou, W., Wang, J., Yang, Y. & Wu, P. Correlated room temperature ferromagnetism and photoluminescence in Ni-doped SnO flower-like architecture synthesized via hydrothermal method. *Mater. Chem. Phys.* **199**, 216–224 (2017).
17. Dai, G., Zhou, W., Ma, X., Yuan, J. & Wu, P. Structure and magnetic properties of Cr-Doped tin monoxide prepared by hydrothermal method. *Ceram. Int.* **46**, 13350–13355 (2020).
18. Vázquez-López, A., Martínez-Casado, R., Cremades, A. & Maestre, D. Effect of Li-doping on the optoelectronic properties and stability of tin (II) oxide (SnO) nanostructures. *J. Alloy. Compd.* **959**, 170490 (2023).
19. Lester, E. et al. Controlled continuous hydrothermal synthesis of cobalt oxide (Co3O4) nanoparticles. *Prog. Cryst. Growth Charact. Mater.* **58**, 3–13 (2012).
20. Makhlouf, S. A., Bakr, Z. H., Aly, K. I. & Moustafa, M. Structural, electrical and optical properties of Co3O4 nanoparticles. *Superlattices Microstruct.* **64**, 107–117 (2013).
21. Farhadi, S., Pourzare, K. & Bazgir, S. Co3O4 nanoplates: Synthesis, characterization and study of optical and magnetic properties. *J. Alloy. Compd.* **587**, 632–637 (2014).
22. Shi, H. & He, X. Large-scale synthesis and magnetic properties of cubic CoO nanoparticles. *J. Phys. Chem. Solids* **73**, 646–650 (2012).
23. Abd-Elrahim, A. G. & Chun, D. M. Fabrication of efficient nanostructured Co_3O_4-Graphene bifunctional catalysts: Oxygen evolution, hydrogen evolution, and H_2O_2 sensing. *Ceram. Int.* **46**, 23479–23498 (2020).
24. Abd-Elrahim, A. G. & Chun, D. M. Facile one-step deposition of Co_3O_4-MoS_2 nanocomposites using a vacuum kinetic spray process for non-enzymatic H_2O_2 sensing. *Surf. and Interfaces* **21**, 100748 (2020).
25. Umemura, R., Ishii, M., Uehara, M. & Kimishima, Y. Magnetic Properties of Transition Metal Doped CuO by Mechanical Milling. *Trans. Mater. Res. Soc. Jpn* **36**, 249–252 (2011).
26. Shaabani, B., Alizadeh-Gheshlaghi, E., Azizian-Kalandaragh, Y. & Khodayari, A. Preparation of CuO nanopowders and their catalytic activity in photodegradation of Rhodamine-B. *Adv. Powder Technol.* **25**, 1043–1052 (2014).
27. Singhal, S., Kaur, J., Namgyal, T. & Sharma, R. Cu-doped ZnO nanoparticles: Synthesis, structural and electrical properties. *Physica B* **407**, 1223–1226 (2012).
28. Hwang, J., Timusk, T. & Gu, G. High-transition-temperature superconductivity in the absence of the magnetic-resonance mode. *Nature* **427**, 714–717 (2004).
29. H. Kumar, R. Rani, Structural and optical characterization of ZnO nanoparticles synthesized by microemulsion route, International Letters of Chemistry, Physics and Astronomy, 14 (2013).
30. Abdullah, W. R. W., Zakaria, A. & Ghazali, M. S. M. Synthesis mechanism of low-voltage praseodymium oxide doped zinc oxide varistor ceramics prepared through modified citrate gel coating. *Int. J. Mol. Sci.* **13**, 5278–5289 (2012).
31. Abu-Elsaad, N. Elastic properties of germanium substituted lithium ferrite. *J. Mol. Struct.* **1075**, 546–550 (2014).
32. El-Taher, A., Abd El Azeem, S. & Ibrahiem, A. Influence of permanent magnet stirring on dendrite morphological and elastic properties of a novel Sn–Ag–Cu–Sb–Al solder alloy by ultrasonic pulse echo method. *J. Mater. Sci.: Mater. Electron.* **31**, 9630–9640 (2020).
33. Sahay, P., Tewari, S., Nath, R., Jha, S. & Shamsuddin, M. Studies on ac response of zinc oxide pellets. *J. Mater. Sci.* **43**, 4534–4540 (2008).
34. Sedky, A., Ali, A. M. & Algarni, H. Structural, FTIR, optical and magnetic investigation of Zn1− xMxO ceramics with M= Cu, Mn: Comparative study. *J. Alloy. Compd.* **912**, 165139 (2022).
35. Muy, S., Schlem, R., Shao-Horn, Y. & Zeier, W. G. Phonon–ion interactions: Designing ion mobility based on lattice dynamics. *Adv. Energy Mater.* **11**, 2002787 (2021).
36. Y. Ben Taher, A. Oueslati, N. Maaloul, K. Khirouni, M. Gargouri, Conductivity study and correlated barrier hopping (CBH) conduction mechanism in diphosphate compound, Appl. Phys. A, 120 (2015) 1537–1543.
37. Gupta, R. et al. Advances in micro and nano-engineered materials for high-value capacitors for miniaturized electronics. *J. Energy Storage* **55**, 105591 (2022).
38. Singh, J. & Singh, R. C. Structural, optical, dielectric and transport properties of ball mill synthesized ZnO–V2O5 nano-composites. *J. Mol. Struct.* **1215**, 128261 (2020).
39. Belkhaoui, C., Mzabi, N., Smaoui, H. & Daniel, P. Enhancing the structural, optical and electrical properties of ZnO nanopowders through (Al+ Mn) doping. *Results in Physics* **12**, 1686–1696 (2019).
40. Bharatiya, D., Parhi, B., Sahu, H. & Swain, S. K. Factors influencing the dielectric properties of GO/MO nanocomposites. *J. Mater. Sci.: Mater. Electron.* **34**, 452 (2023).
41. Omri, K., Bettaibi, A., Khirouni, K. & El Mir, L. The optoelectronic properties and role of Cu concentration on the structural and electrical properties of Cu doped ZnO nanoparticles. *Physica B* **537**, 167–175 (2018).
42. Munawar, T., Iqbal, F., Yasmeen, S., Mahmood, K. & Hussain, A. Multi metal oxide NiO-CdO-ZnO nanocomposite–synthesis, structural, optical, electrical properties and enhanced sunlight driven photocatalytic activity. *Ceram. Int.* **46**, 2421–2437 (2020).
43. Ansari, S. A., Nisar, A., Fatma, B., Khan, W. & Naqvi, A. Investigation on structural, optical and dielectric properties of Co doped ZnO nanoparticles synthesized by gel-combustion route. *Mater. Sci. Eng., B* **177**, 428–435 (2012).
44. Hassan, M. M. et al. Structural and frequency dependent dielectric properties of Fe3+ doped ZnO nanoparticles. *Mater. Res. Bull.* **47**, 3952–3958 (2012).
45. Singh, J. & Singh, R. C. Tuning of structural, optical, dielectric and transport properties of Fe-doped ZnO: V system. *Mater. Sci. Semicond. Process.* **121**, 105305 (2021).
46. Sahay, P., Mishra, R., Pandey, S., Jha, S. & Shamsuddin, M. Structural, dielectric and photoluminescence properties of co-precipitated Zn-doped SnO2 nanoparticles. *Curr. Appl. Phys.* **13**, 479–486 (2013).
47. N. Manjula, G. Selvan, R. Perumalsamy, R. Thirumamagal, A. Ayeshamariam, M. Jayachandran, Synthesis, structural and electrical characterizations of SnO 2 nanoparticles, International Journal of Nanoelectronics & Materials, 9 (2016).

48. Kumari, N., Ghosh, A. & Bhattacharjee, A. Investigation of structural and electrical properties of CuO modified SnO2 nanoparticles. *Mater. Sci. Semicond. Process.* **19**, 114–123 (2014).
49. Sagadevan, S. & Podder, J. Investigation on structural, surface morphological and dielectric properties of Zn-doped SnO2 nanoparticles. *Mater. Res.* **19**, 420–425 (2016).
50. Abd-Elrahim, A. G., Sedky, A., Afify, N. & Abbas, A. The effect of composition on the structure, optical, and room-temperature ferromagnetic properties of hydrothermally synthesized (ZnSn) 1-xCuxO nanocomposites. *Physica B* **674**, 415568 (2024).
51. Sedky, A., Afify, N., Abbas, A. & Abd-Elrahim, A. G. Cooperative effects due to Zn–Sn replacement by Co-ions on the optical and magnetic properties of (ZnSn) 1-xCoxO nanocomposites. *Mater. Chem. Phys.* **313**, 128776 (2024).
52. Abd-Elrahim, A. G. & Chun, D.-M. Facile one-step deposition of ZnO-graphene nanosheets hybrid photoanodes for enhanced photoelectrochemical water splitting. *J. Alloy. Compd.* **870**, 159430 (2021).
53. Abd-Elrahim, A. G. & Chun, D. M. Room-temperature deposition of ZnO-graphene nanocomposite hybrid photocatalysts for improved visible-light-driven degradation of methylene blue. *Ceram. Int.* **47**, 12812–12825 (2021).
54. Othman, A. A., Osman, M. A., Ibrahim, E. M. M., Ali, M. A. & Abd-Elrahim, A. G. Mn-doped ZnO nanocrystals synthesized by sonochemical method: Structural, photoluminescence, and magnetic properties. *Mater. Sci. Eng. B-Adv. Funct. Solid-State Mater.* **219**, 1–9 (2017).
55. Raja, K., Ramesh, P. S. & Geetha, D. Structural, FTIR and photoluminescence studies of Fe doped ZnO nanopowder by co-precipitation method. *Spectrochim. Acta Part A Mol. Biomol. Spectrosc.* **131**, 183–188 (2014).
56. Madbouly, A. I., Morsy, M. & Alnahdi, R. F. Microwave-assisted synthesis of Co-doped SnO2/rGO for indoor humidity monitoring. *Ceram. Int.* **48**, 13604–13614 (2022).
57. A. Sedky, A.M. Abd-Elnaiem, M. Al-Dossari, N.S. Abd El-Gawaad, N. Afify, G. Abbady, Enhancement of mechanical and ferromagnetic properties of Cd0.4Mn0.6XO nanocomposites (X=ZnO, SnO, CuO, Al2O3, Fe2O3, CoO, NiO), Materials Science and Engineering: B, 310 (2024) 117737.
58. Sedky, A., Ali, A. M. & Algarni, H. Structural, FTIR, optical and dielectric properties of Zn1-xAlxO ceramics for advanced applications. *Opt. Quant. Electron.* **54**, 376 (2022).
59. A. Sedky, N. Afify, M. Omer, M. Sayed, A.M. Ali, A. Almohammedi, Annealing temperature effect on structural, mechanical, and magnetic properties of Cd0. 40M0. 60ZnO2 (M= Mn, Ni) nanocomposites, Materials Chemistry and Physics, 309 (2023) 128326.
60. El-Taher, A., Abd El Azeem, S. & Ibrahiem, A. Novel low Ag-content Sn–Ag–Cu–Sb–Al solder alloys with enhanced elastic compliance and plastic energy dissipation ability by applying rotating magnetic field. *J. Mater. Sci.: Mater. Electron.* **32**, 6199–6213 (2021).
61. A. Sedky, N. Afify, M. Omer, M.A. Sayed, A.M. Ali, A. Almohammedi, Annealing temperature effect on structural, mechanical, and magnetic properties of Cd0.40M0.60ZnO2 (M = Mn, Ni) nanocomposites, Materials Chemistry and Physics, 309 (2023) 128326.
62. Abd-Elrahim, A. G. et al. Sonochemical synthesis of mesoporous ZnyCd1-yS quantum dots: Composition-dependent optical, electrical, dielectric, and hydrogen-generation characteristics. *J. Phys. Chem. Solids* **197**, 112414 (2025).
63. A. Sedky, A. Almohammedi, N. Afify, G. Abbady, Negative dielectric constant and multi-visible photolumenses emissions of Cd (1-x) CoxO nanocomposites with (0.00≤ x≤ 1.00), Inorg. Chem. Commun., 163 (2024) 112301.
64. Sundararajan, M., Sakthivel, P. & Fernandez, A. C. Structural, optical and electrical properties of ZnO-ZnS nanocomposites prepared by simple hydrothermal method. *J. Alloy. Compd.* **768**, 553–562 (2018).
65. Vinosha, P. A. et al. Investigation of optical, electrical and magnetic properties of cobalt ferrite nanoparticles by naive co-precipitation technique. *Optik* **127**, 9917–9925 (2016).
66. Samuel, M. S., Koshy, J., Chandran, A. & George, K. Dielectric behavior and transport properties of ZnO nanorods. *Physica B* **406**, 3023–3029 (2011).
67. Nakayama, M., Nogami, M., Yoshida, M., Katsumata, T. & Inaguma, Y. First-Principles Studies on Novel Polar Oxide ZnSnO3; Pressure-Induced Phase Transition and Electric Properties. *Adv. Mater.* **22**, 2579–2582 (2010).
68. N.A. All, A. Sedky, M. Mohamed, N. Afify, G. Khouqeer, M. Almokhtar, An investigation for optical, photocatalytic, photoluminescence and dielectric properties of Cd0.40Ni0.60ZnO2 annealed nanocomposites, J. Alloy. Compd., 990 (2024) 174432.
69. Wu, W., Huang, X., Li, S., Jiang, P. & Toshikatsu, T. Novel three-dimensional zinc oxide superstructures for high dielectric constant polymer composites capable of withstanding high electric field. *J. Phys. Chem. C* **116**, 24887–24895 (2012).
70. Dridi, R. et al. Electrical conductivity of Zn2SnO4 thin films along with wettability and EtOH-sensing. *J. Alloy. Compd.* **708**, 769–779 (2017).
71. Mhamdi, A., Ouni, B., Amlouk, A., Boubaker, K. & Amlouk, M. Study of nickel doping effects on structural, electrical and optical properties of sprayed ZnO semiconductor layers. *J. Alloy. Compd.* **582**, 810–822 (2014).
72. Asami, K. Characterization of heterogeneous systems by dielectric spectroscopy. *Prog. Polym. Sci.* **27**, 1617–1659 (2002).
73. Nasrallah, D. A., El-Metwally, E. G. & Ismail, A. M. Structural, thermal, and dielectric properties of porous PVDF/Li4Ti5O12 nanocomposite membranes for high-power lithium-polymer batteries. *Polym. Adv. Technol.* **32**, 1214–1229 (2021).
74. Abd-Elrahim, A. G., Chun, D.-M., Ibrahim, E. & Ali, M. A. Sonochemical-assisted preparation of mesoporous ZnS quantum dots: Optical, electrical, and temperature-dependent dielectric characteristics. *Physica B* **670**, 415408 (2023).
75. M.A. .Ali, D.-M. Chun, E. Ibrahim, A.G. Abd-Elrahim, Optical and temperature-dependent electrical and dielectric properties of ultrasound-synthesized CdS quantum dots, Physica Scripta, (2023).
76. Othman, A., Osman, M., Ali, M. A. & Ibrahim, E. Influence of doping with Sb3+, In3+, and Bi3+ ions on the structural, optical and dielectric properties of ZnS nanoparticles synthesized by ultrasonication process. *Physica B* **614**, 413041 (2021).
77. H. Bouaamlat, N. Hadi, N. Belghiti, H. Sadki, M. Naciri Bennani, F. Abdi, T.-d. Lamcharfi, M. Bouachrine, M. Abarkan, Dielectric properties, AC conductivity, and electric modulus analysis of bulk ethylcarbazole-terphenyl, Advances in Materials Science and Engineering, 2020 (2020) 8689150.
78. Abdullah, M. Consequences of frequency and temperature on the ac-conductivity in ε-GaSe semiconductor single crystal. *Results in Physics* **25**, 104220 (2021).
79. Mandurah, M. M., Saraswat, K. C. & Kamins, T. I. A model for conduction in polycrystalline silicon—Part II: Comparison of theory and experiment. *IEEE Trans. Electron Devices* **28**, 1171–1176 (1981).
80. Farooq, M. I., Khan, M. S., Yousaf, M., Zhang, K. & Zou, B. Antiferromagnetic magnetic polaron formation and optical properties of CVD-grown Mn-doped zinc stannate (ZTO). *ACS Appl. Electron. Mater.* **2**, 1679–1688 (2020).
81. Singh, J., Virpal, V., Sharma, S. & Singh, R. C. *in: AIP Conf* (AIP Publishing, 2017).
82. S.M. Soosen, A. Chandran, J. Koshy, K. George, Correlated barrier hopping in ZnO nanorods, J. Appl. Phys., 109 (2011).
83. Ram, M., Bala, K., Sharma, H. & Negi, N. *in: AIP Conf* (AIP Publishing, 2016).
84. Xing, C. et al. Phonon characteristics, crystal structure, and intrinsic properties of a Y (Mg 1/2 Sn 1/2) O 3 ceramic. *RSC Adv.* **7**, 35305–35310 (2017).
85. Ahmad, F. & Maqsood, A. Complex impedance, dielectric constant, electric modulus, and conductivity analysis of Cd doped ZnO nanostructures at high temperatures. *Physica E* **143**, 115353 (2022).
86. S. Das Sarma, E. Hwang, Short-range disorder effects on electronic transport in two-dimensional semiconductor structures, Physical Review B, 89 (2014) 121413.
87. Hammami, H., Arous, M., Lagache, M. & Kallel, A. Experimental study of relaxations in unidirectional piezoelectric composites. *Compos. A Appl. Sci. Manuf.* **37**, 1–8 (2006).

88. Chaari, M. & Matoussi, A. Electrical conduction and dielectric studies of ZnO pellets. *Physica B* **407**, 3441–3447 (2012).

Funding
This work was supported and funded by the Deanship of Scientific Research at Imam Mohammad Ibn Saud Islamic University (IMSIU; grant number IMSIU-DDRSP2502).

Declarations

Competing interests
The authors declare that they have no conflict of interest.

Ethical approval
The present manuscript is original work and has never been under evaluation for any other journal.

Additional information
Correspondence and requests for materials should be addressed to A.S. or A.G.A.-E.

Reprints and permissions information is available at www.nature.com/reprints.

Publisher's note Springer Nature remains neutral with regard to jurisdictional claims in published maps and institutional affiliations.